for CFAI

Computation of External Aerodynamics for a Canard Rotor/Wing Aircraft

S. Pandya and M. J. Aftosmis
Abstract for 39th AIAA Aerospace Sciences Meeting and Exhibit
Reno, NV, Jan. 2001

1.0 Abstract

The aerodynamic loads on a Canard Rotor/Wing vehicle are investigated using inviscid numerical simulations to understand the aerodynamic characteristics of the vehicle during conversion from rotorcraft to fixed wing flight. Steady numerical simulations at five azimuthal rotor indices are presented over a quarter turn of the rotor, producing 19 points during a single rotation due to symmetry. A Cartesian mesh approach is used to compute the steady flow field. All computations are done with a faired over engine inlet and exit to be
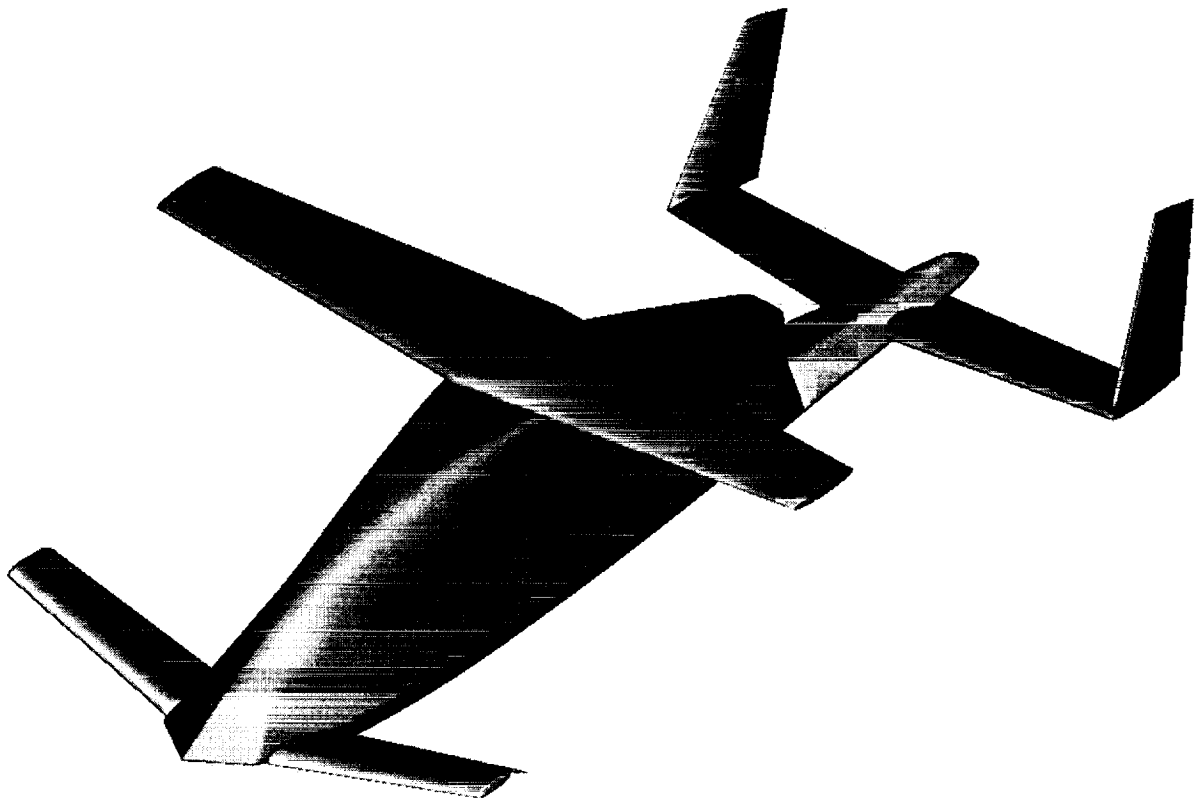
FIGURE 1. The geometry of a generic Canard Rotor/Wing(CRW) aircraft

consistent with the wind tunnel model geometry. Modification to the geometry is suggested and the aerodynamic effect of the modification is discussed.

2.0 Introduction

The Canard Rotor/Wing(CRW) is a vertical takeoff and landing aircraft(see Figure 1). A two bladed rotor with elliptic airfoil sections is used for takeoff, hover, and landing. It is similar to the X-wing prototype in that it uses a rotor to takeoff and land vertically and then puts the rotor in a fixed position during forward flight. Like the X-wing, the concept uses the rotor as wing(s) to generate the lift needed to keep the aircraft aloft during high speed forward flight.

However, the X-wing concept encounters controllability problems during conversion. This is due to the fact that the rotor must produce all the lift to keep the aircraft afloat during conversion from rotory to fixed wing flight.

In contrast, the CRW's rotor is unloaded during conversion from rotory to fixed wing flight because the weight of the aircraft is carried by the canard and the horizontal tail. The presence of the canard surface has the advantage that the decelerating rotor does not have to produce lift.

The challenge then is to accurately predict the flight worthiness of the CRW during conversion. One of the issues requiring attention is the forces and moments on the vehicle during conversion(i.e. whether it will fly and how much it will vibrate). Another important issue is to find out if there is enough control authority from the control surfaces to overcome the aerodynamic moments imposed on the aircraft.

To address thess concerns, we run a CFD simulation of the conversion process to compare to the wind tunnel tests. During the final stages of conversion to fixed wing flight, the rotor is not turning very fast. The rotation time scale is much smaller than that of the flow and so the time scales of the flow are dominant. For this reason, we should be able to get a respectable understanding of the flow field by simply fixing the rotor in several positions and computing the steady flow field for each of the rotor settings.

The chosen rotor positions are $0°$, $15°$, $30°$, $45°$, and $90°$. These five rotor positions are used for steady computations at Mach number of 0.196 and angle of attack of $0°$. Each of the computations is performed using the Cartesian mesh flow simulation package of reference [1]. The surface preparation, surface triangulation and Cartesian mesh generation capabilities in this package are used to generate the mesh systems for each of the five cases. An inviscid flow solver for unstructured Cartesian meshes is used to compute the flow. This solver is documented in [2]. We expect that as is often the case, the inviscid results will be a good indication of the forces and moments due to pressure.

This abstract presents the preliminary solutions obtained on the CRW, and discusses the conclusions drawn from these solutions. The effect of the hemispherical rotor hub is especially significant and can explain the forces and moments generated on the vehicle. A geometry change in the hub region is suggested, and the inviscid solutions on the modified

geometry are used to illustrate an aerodynamic trend. A brief description of the methods used is also presented.

A comparison with experimental data[4] and another CFD code will also be included in the paper in order to validate the solution.

3.0 Methods

The process begins with receiving geometry components as CAD solids. The components can be moved, and/or rotated with respect to each other in order to perform parametric studies. In the current case, this feature helped rotate the rotor into several different positions. The CAD solids are normally triangulated first. However, the CRW geometry was received as a set of parts in the plot3d style surface definition. These parts are shown by different colors in Figure 2. Each part of the CRW is triangulated individually by breaking up the quadrilaterals on the surface into triangles.

The part triangulations are then patched together into one configuration triangulation. The intersection program in the Cartesian package[1] incorporates adaptive precision arithmetic, and includes an automatic tie-breaking routine that consistently resolves geometric degeneracies without user intervention. This tool computes the intersections between closed body triangulations, and retriangulates the intersection neighborhood to join the pieces together into a single triangulation.

The volume mesh generation algorithm takes the intersected surface triangulation as input. This program generates an unstructured Cartesian mesh through subdivision of hexahedral cells of an initially uniform coarse grid. It adapts to the contours of the geometry, thus creating a mesh where the size of the cubic cells is smallest in the neighborhood of the sharpest features of the geometry, while away from the geometry, the grid remains coarse. Specific regions of enhancement can also be defined in order to ensure that a given mesh size is maintained in a specified area. The program also computes the intersections of the geometry with the cells of the mesh which pierce the geometry in order to define polyhedral cut-cells. The faces of these polyhedral cells are then used to specify the tangency boundary condition in the flow solver. An example of a mesh generated by this algorithm is presented in Figure 2. The approach in this volume mesh generator preserves the ability to refine the mesh to different degrees in different directions. This makes it possible to avoid generating an excessive number of Cartesian cells in three dimensions.

A Cartesian flow solver that solves the Euler equations is used to compute the flow field. The Euler equations describe the unsteady flow of an inviscid perfect gas and may be expressed in integral form.

$$\int\int_{\Omega} \frac{\partial U}{\partial t}\, d\Omega = -\oint_{\partial\Omega} F \bullet \vec{n}\, dS$$

Here U is the state vector of conserved quantities, and F is the tensor of flux density for an inviscid perfect gas. Ω refers to an arbitrary control volume and $\partial\Omega$ is its closed boundary with an outward facing surface vector $\vec{n}$.
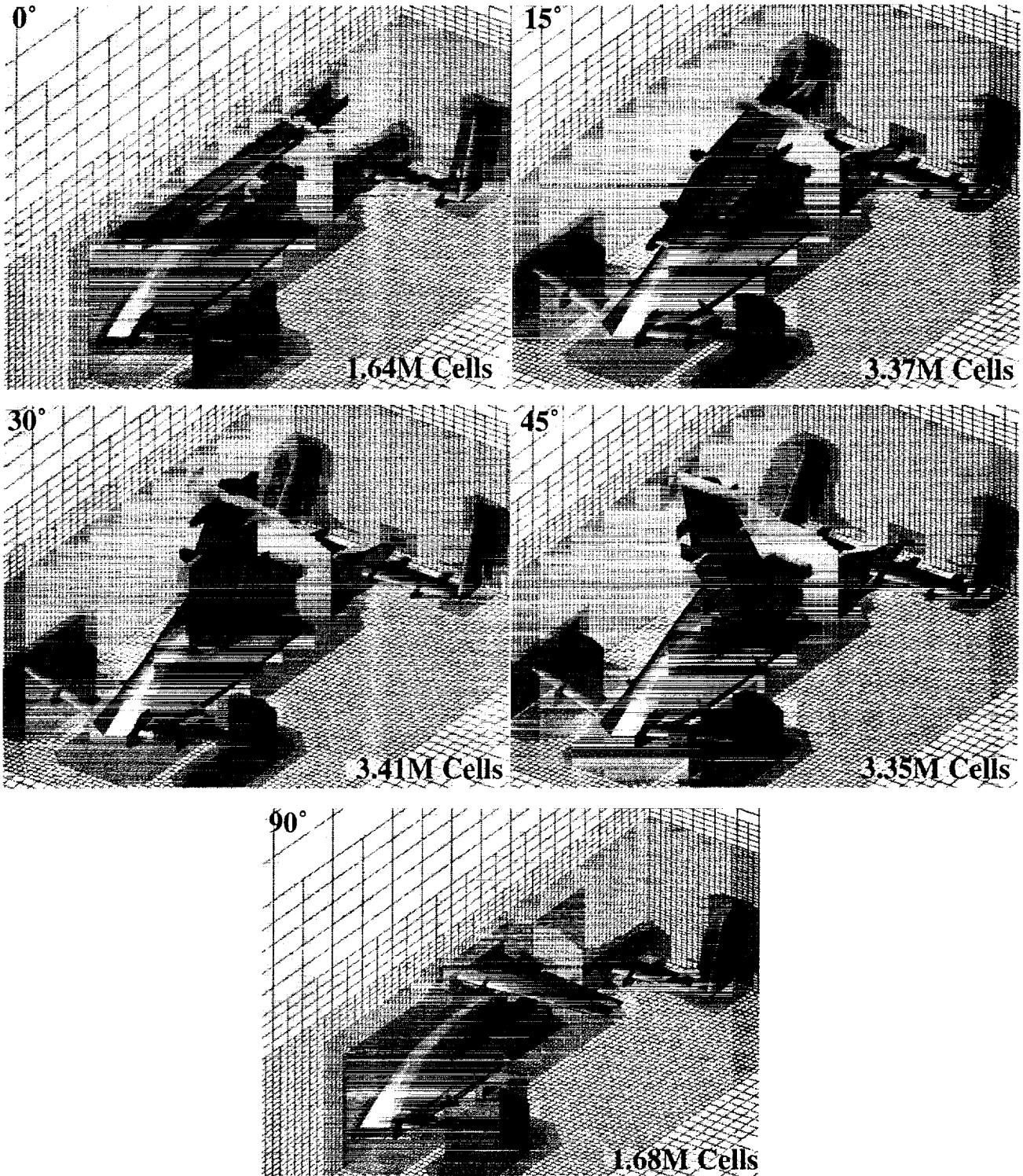
FIGURE 2. The volume mesh over the CRW

The integration method uses a cell centered discretization with computational control volumes formed by the vertices of Cartesian grid cells. An explicit multi-stage modified Runge-Kutta algorithm advances the central difference spatial discretization forward in

time. Local time-stepping is implemented for faster convergence for steady flows. The scheme uses blended 2nd and 4th difference dissipation found in many central difference codes. This flow solver scheme has its origin in Ref. [3]. This flow solver is well documented in the literature. Ref. [2] provides a complete description.

4.0 Solutions

The solutions are presented below for all rotor settings at a Mach number of 0.196 and zero angle of attack. The boundaries spanned 20 times the body length in all directions. For the rotor settings 0° and 90°, the geometry and flow are symmetric about the midplane, so only half of the flow field is computed with the assumption that the other half is a mirror image of the computed flow field. The mesh size for these half-body cases was approximately 1.6 million vertices. The rest of the cases were computed with a mesh surrounding the entire body since no assumptions of symmetry can be made for these rotor positions. The mesh size for these cases was approximately 3.5 million vertices.

First, the convergence behavior for a typical run is presented. The convergence behavior of the lift for the 90° rotor position case is shown in Figure 3 along with a running average and a standard deviation. Each of the solutions is converged up to a point where the value of the lift settles to within 2% standard deviation. The ringing in the value of the lift is unsettling at first, but can clearly be attributed to two of the features in the flow. One of these is an axial vortex behind the hub which is present due to the separation from the hemispherical body of the hub. This unsteady feature in the flow field along with a separation region resulting from a backwards facing step (faired over engine nozzle) makes the

CRW Lift Convergence
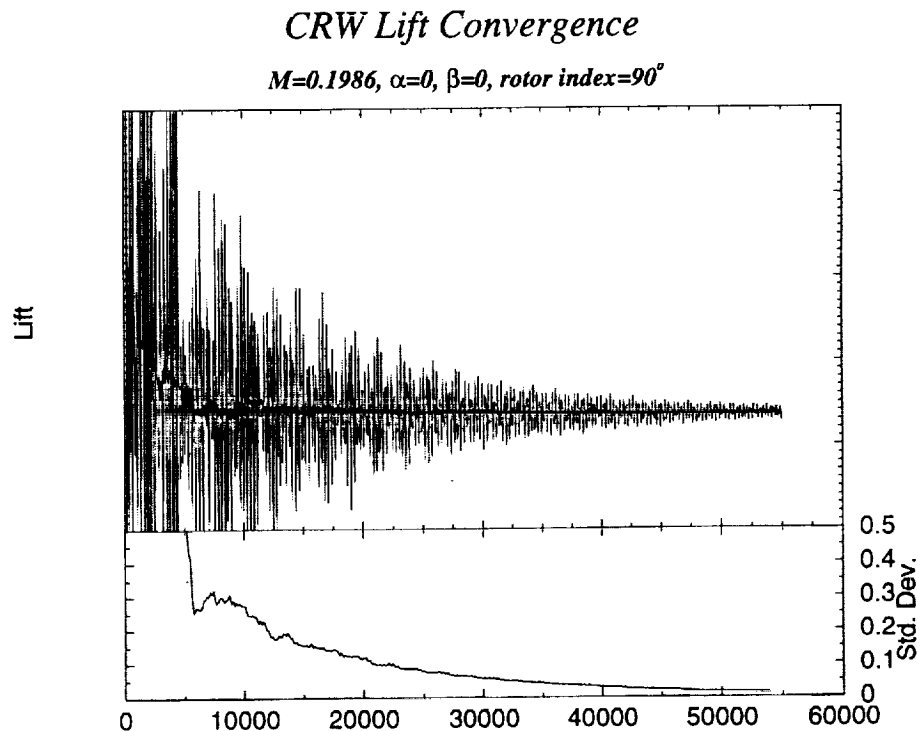
M=0.1986, α=0, β=0, rotor index=90°

FIGURE 3. History of lift with respect to iteration number

value of the lift sensitive to the changes in these features from one iteration step to the next. The iterative process is damping the motion of the features, however, and the mean as shown by the running average is settling to a value. In other words, the standard deviation is getting very small. Similar behavior is seen in the other forces, but the lift has the worst behavior. The moments also show a similar ringing and pitching moment is the most sensitive. When the standard deviation for the lift is close to 1%, the pitching moment is just getting below 5%.

FIGURE 4. Surface pressure on the CRW for five rotor positions

4.1 Force and moment variation with respect to rotor azimuth angle

We begin our search for trends with the surface pressure. In an inviscid analysis, the surface pressure should tell the story of the forces being imparted onto the body. The body of the CRW colored by the coefficient of pressure is shown in Figure 4 for all the different rotor positions. The suction(shown in red) on the top surface shows that the canard/flap and the horizontal tail are the two components producing lift. It can also be seen that the rotor produces little or no lift as expected at this condition. When we look at this figure closely, we realize that most of the surface pressures do not change from rotor position to rotor position. However, the hub under the rotor seems to have a large low pressure region which changes with the changing rotor position as shown in Figure 6 on page 9.

The trends of the flow can be best examined if we look at the variations in forces and moments with respect to the azimuthal position of the rotor and correlate them to the visible changes in pressure on the surface. The plots of the forces and moments with respect to the azimuthal position are presented in Figure 5. The trends seen in these force and moment plots can be explained in terms of the differences in the flow for the solutions in question. The surface pressures on different parts of the configuration match considerably well except in the region of the rotor hub fairing. Therefore, the major factor dominating the force and moment behavior must be related to the suction on the rotor hub fairing assembly. This strong suction is the result of the flow accelerating around the hub. From the surface pressure figures we note that the peak suction follows the rotor's azimuthal progress. The variations in the suction acting on the horizontal and vertical surfaces around the hub correlate with the overall vehicle forces and moments.

The plot of lift with respect to the azimuthal angle shows that more lift is being generated when the rotor is in the $0°$ position. This can be explained if we look at the suction in the hub area. In this area the suction follows the position of the rotor. To take a closer look at the suction behavior in the hub area, we use figure 6. This figure shows the surface pressure from the underside of the wing so that the hub region is readily visible. We observe that the largest suction on the hub is created when the rotor is in the $90°$ position. This suction generates a large negative lift on the rotor/hub assembly, which contributes to a lower total lift. In the $0°$ case, when the rotor is aligned with the body, the lift on the rotor/hub assembly is still negative. However, the magnitude is much smaller and so this case has a larger total lift. As the suction follows the rotor, the lift varies between these two extremes.

The variation in the drag force is much smaller and other effects such as the separated flow behind the hub and the engine exit may be the primary causes of drag variation. In order for the suction in the hub region to have a direct effect on the drag force, vertical surfaces facing the direction of the flow or away from it are needed and these do not exist in the vicinity of the hub. Thus, the movement of the suction in the hub region does not have a large effect on the drag.
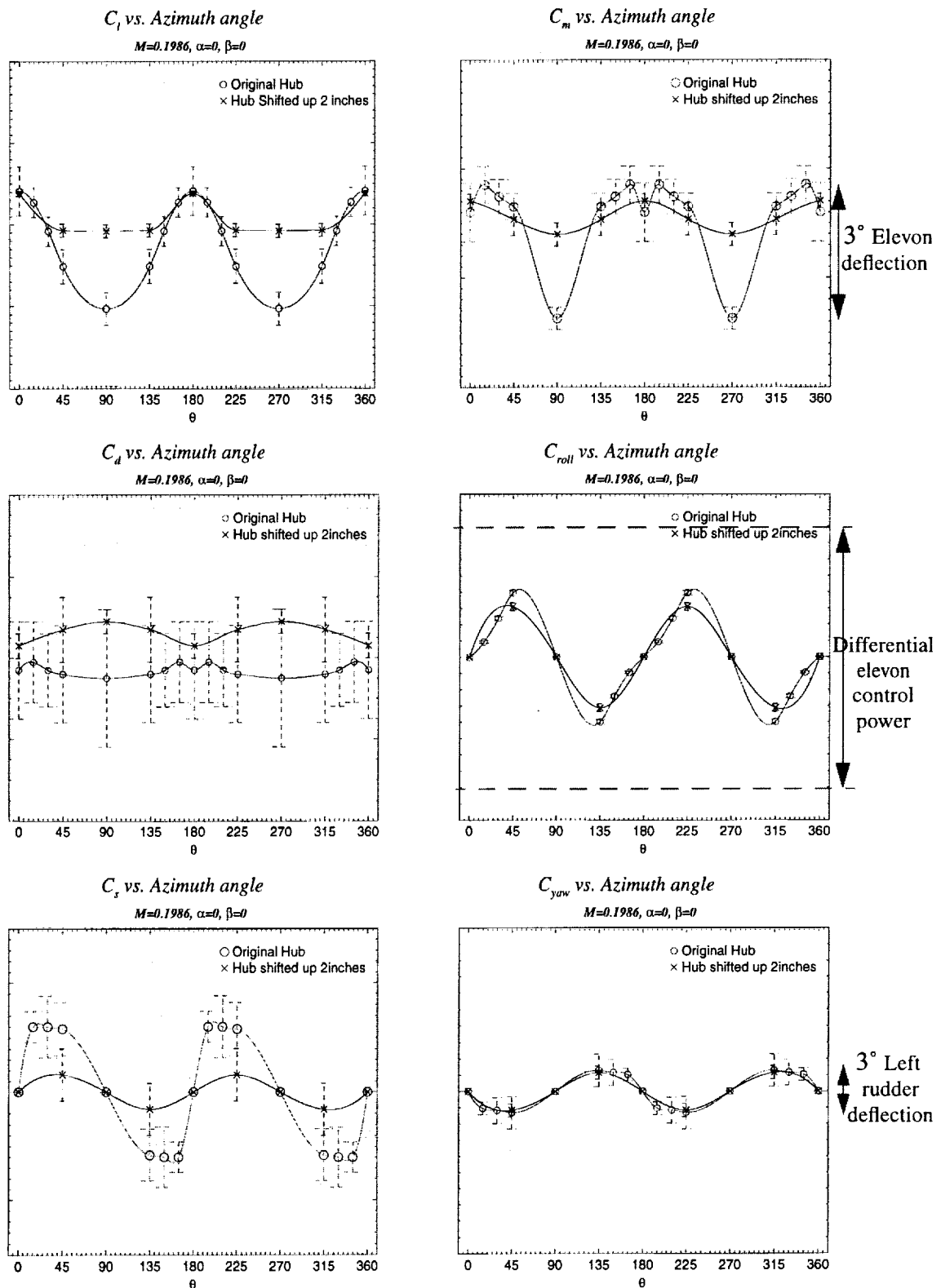
FIGURE 5. Forces and moments with respect to the rotor position

The Side force can also be explained by the tendency of the suction to follow the rotor. In this case, when the rotor is in the 0° or the 90° positions, the flow is symmetric and the side force is zero. However, in all other cases, the side force is non zero due to the fact that the suction is higher on one side of the body than the other and acts on the vertical surfaces below the hub. The sign of the side force can also be explained by the suction from the hub. If we look at the 45° case in Figure 6, we see a larger amount of suction on the back rotor as compared to the suction under the front rotor. The result is a positive side force. This is confirmed in Figure 5 where the side force is indeed positive at 45° rotor position. The 45° case should be the same as the 135° case, but with the opposite effects since the rotor is on the other side of the body. Thus, the value of the side force for the 135° case
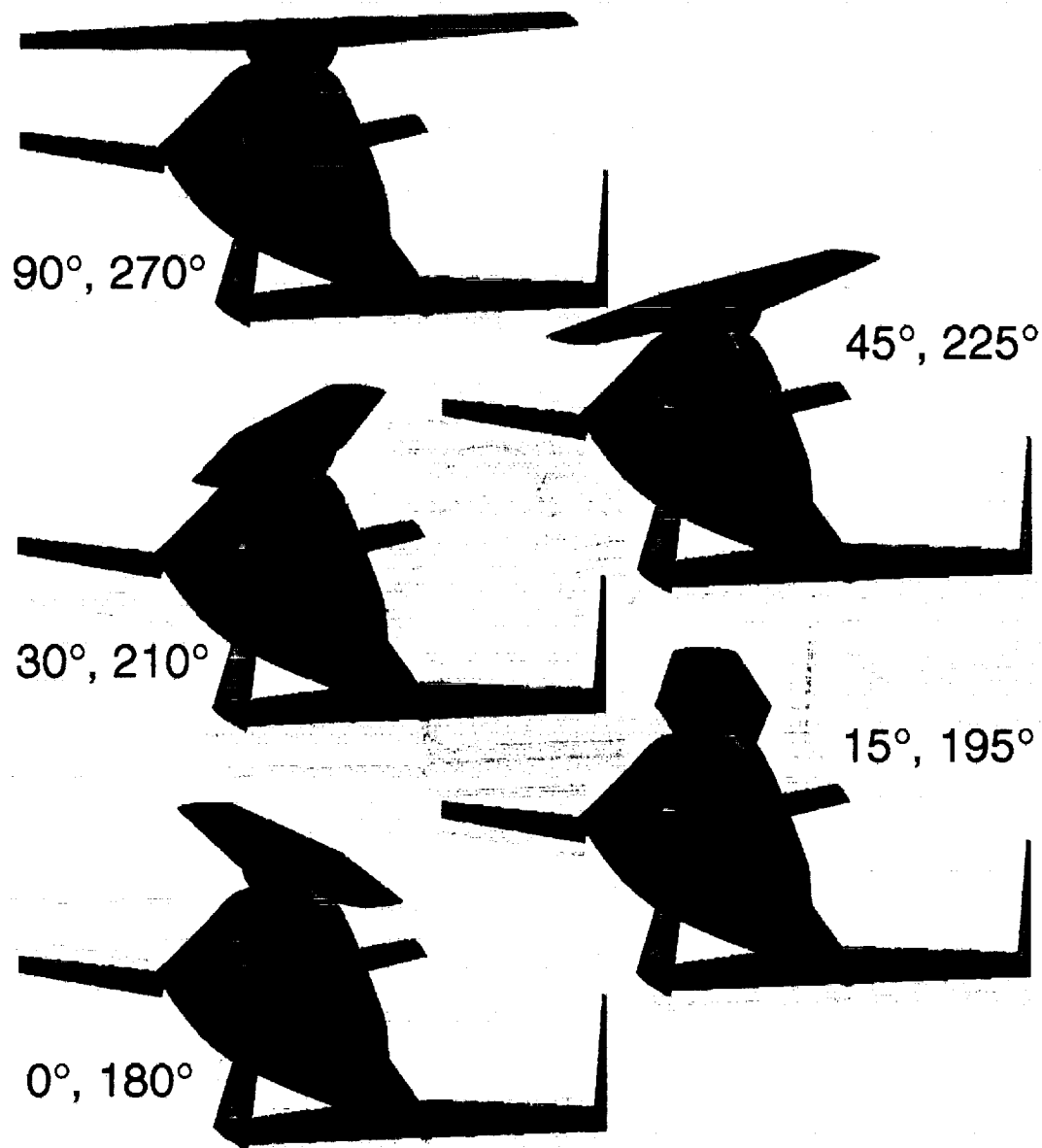

FIGURE 6. Underview of the surface pressure

should be negative of the 45° case. The logic carries over to the rest of the cases between 90° and 180° and again between 270° and 360°. The values between 180° and 270° should be duplicates of the values between 0° and 90°.

The variation of the moment with respect to the azimuthal angle of the rotor can also be explained in terms of the suction created by the hub. The suction on the hub, once again, follows the rotor. Thus at a rotor position of 45°, the suction is greater close to where the rotor is. However, due to the oncoming flow, the suction in the front is relieved and so closer to the front facing rotor, there is less suction than the back side. This contributes to a larger downward force on the rearward swept rotor which in turn contributes to a more positive pitching moment.

The rolling moment also depends on the hub suction behavior. Once again, we compare the 0°, the 45° and the 90° cases. At 0 and 90 degrees, the rolling moment is zero due to the symmetry of the flow. However, at 45°, the suction has clearly caused the right rotor to produce less lift than the left rotor. For this reason, there is a positive rolling moment produced. Similarly, a positive rolling moment is produced for the 15°, and 30° cases. Like the side force, the symmetry of the flow dictates the sign of the moment at other conditions.

A small yawing moment is produced due to the suction force acting differentially on the vertical surfaces close to the hub and its sign can also be explained in terms of the hub suction.

Based on the above analysis, it seems to make engineering sense to relieve the suction due to the hemispherical hub. One obvious solution is to shorten the size of the hub so that a gap is left close to the fuselage allowing the flow to pass through. This modification to the gometry is made in our model and the results of the midification are also plotted in Figure 5 on page 8.

Figure 5 shows dramatic improvement in the variation of the lift, side force and pitching moment. This shows an improvement in the amount of vibration the aircraft goes through in a given cycle of the rotor. It also improves the longitudinal stability of the aircraft.

However, it fails to make a large impact on the lateral stability character of the craft. This is true because the suction on the underside of the rotor seen in Figure 6 on page 9 is still present due to the presence of the hub. The change in size of the hub does improve the lateral character of the aircraft, but the difference is not large.

5.0 Concluding remarks

The vehicle loads on the CRW were evaluated during the conversion process using computational tools for inviscid analysis with a Cartesian mesh. The resulting trends in forces and moments were explained in terms of the forces imparted on the body due to aerodynamic pressure.

It was confirmned that the rotor is indeed unloaded or close to unloaded during conversion. It was also confirmed that the load of the aircraft can be carried by the canard and

the horizontal tail. Plots of the variation of the forces and moments with respect to the rotor position were generated and explained in terms of the varying suction in the rotor hub fairing region.

The simulations and the investigation of the cause of the variation in the forces and moments suggest that smaller forces and moments will be imparted to the geometry if the gap between the rotor hub and the upper fuselage is increased. This is verified through investigation of a geometry with a hub which leaves room between the fuselage and the hub. It is found that while the smaller hub substantially improves the longitudinal character of the aircraft, the lateral characteristics do not change dramatically. Removing the hub entirely or the design of a non-rotating aerodynamically shaped hub should also be considered.

In addition to the information in this abstract, the final paper will include analysis of the aircraft without the hub in order to confirm the present conclusions. We will also include a comparison with wind tunnel experiment.

References

1. Aftosmis, M. J., Berger, M. J., Melton, J. E., *Robust and efficient Cartesian mesh generation for component-based geometry*, AIAA Paper 97-0196, Jan. 1997.

2. Melton, J., Thomas, S., and Cappucio, G. *Unstructured Euler flow solutions using hexahedral call refinement*, AIAA Paper 91-0637.

3. Jameson, A. and Baker, T. J., *Solution of the Euler equations for complex configurations*, AIAA Paper 83-1929CP.

4. McDonnell Douglas Helicopter Systems, *Dragonfly advanced technology demonstration, Canard Rotor/Wing ; Fixed-wing wind tunnel test report*, Document 98ADRL-B2288-WTTR-009, May 1999.